Balancing the marine sulfur cycle

D.L. Johnson[1*], **J.F. Adkins**[1]

[1]Division of Geological & Planetary Sciences, California Institute of Technology, 1200 E California Blvd, Pasadena, CA 91125

Key Points:

- Cluster analysis identifies geographically distinct pore-water [SO_4^{2-}] profiles
- Pyrite literature compilation confirms shelf and slope dominate global burial
- Sampling and measurement biases can account for prior imbalance in S flux estimates

*Current address: Department of Earth, Environmental and Planetary Sciences, Rice University, 6100 Main St., MS-126, Houston, TX 77005

Corresponding author: D.L. Johnson, Dan.Johnson@rice.edu

Abstract

Sulfate (SO_4^{2-}) reduction is a major SO_4^{2-} output flux from Earth's oceans, but an imbalance between recent estimates of this flux and corresponding input fluxes suggests inaccuracy in our understanding. Here, we combine global geographic trends in aqueous and dissolved-phase sedimentary data to resolve this inaccuracy. [SO_4^{2-}] profiles from 700+ sites partition into geographically-distinct k-means clusters based on net sulfate reduction rate (nSRR). Pairing nSRRs with literature-derived pyrite accumulation rates confirms that shelf and slope pyrite burial dominate burial globally. Our results also suggest that sampling and measurement biases have led to erroneously high prior global output estimates and can account for the flux imbalance. Disparate mean $\delta^{34}S$ values for shelf versus deeper ocean pyrite indicate that sea level change may be an overlooked mechanism for forcing past changes in seawater $\delta^{34}S$.

Plain Language Summary

The marine sulfur (S) cycle helps regulate Earth's atmospheric O_2 concentrations and is commonly assumed to operate in a steady-state condition over millions of years. However, recent input and output flux estimates differ by a factor of three, suggesting a drawdown of marine sulfate (SO_4^{2-}) concentrations. We reexamine one of the main output fluxes (pyrite, FeS_2) by combining pore water and solid phase data from seafloor sediments. Distinct geographic trends in these data allow us to make a new output flux estimate compatible with a concentration steady-state in the marine S cycle. Our analysis suggests that sea level changes may have affected our records of the ancient S cycle and resulting estimates of past O_2 concentrations.

1 Introduction

The marine sulfur (S) cycle plays critical roles in regulating ocean-atmosphere O_2 concentrations (Berner, 2005) and balancing CO_2 releases associated with terrestrial sulfide oxidation (Torres et al., 2014). The burial of iron sulfide minerals (e.g. pyrite, FeS_2) formed through the reaction of sedimentary iron with aqueous sulfide derived from sulfate (SO_4^{2-}) reduction acts as a key process within both of these roles. Here, electrons are transferred from organic matter to sulfate via the following simplified stoichiometry:

$$2\,CH_2O + SO_4^{2-} + 2\,H^+ \longrightarrow H_2S + 2\,CO_2 + 2\,H_2O \quad (1)$$

$$H_2S + Fe^{2+} + S_0 \longrightarrow FeS_2 + 2\,H^+ \quad (2)$$

Although previous studies (Alt & Burdett, 1992; Puchelt & Hubberten, 1980; Zak et al., 1980; Sweeney & Kaplan, 1980; Goldhaber & Kaplan, 1974; Scharff, 1980; Bonnell & Anderson, 1987; Böttcher et al., 2004; A. Migdisov et al., 1980; A. A. Migdisov et al., 1983; Lein et al., 1976; Krouse et al., 1977; Johnston et al., 2008; Vinogradov et al., 1962; Kaplan et al., 1963; Sweeney, 1972; Thode et al., 1960; Kaplan et al., 1960; Lein, 1983; Hartmann & Nielsen, 2012; A. A. Migdisov et al., 1974) have revealed significant diversity in the character of S cycling across global deep ocean sediments, most have focused on samples collected from a narrow geographic range. A need for better integration of data from multiple regions into assessments of the modern marine S cycle is underscored by a factor of ∼3 imbalance between recent global net SO_4^{2-} reduction rate (nSRR) estimates (11.3 Tmol/yr (Bowles et al., 2014)) and the pre-anthropogenic riverine input flux of SO_4^{2-} (2.8±0.4 Tmol/yr; (Burke et al., 2018)). If the pre-anthropogenic S cycle was approximately in steady state, such imbalance suggests that this nSRR estimate is too high and that prior S output estimates (Berner, 1982) are more accurate. Alternatively, the marine S cycle could be out of steady state or input fluxes from rivers and assumed minor sources (e.g. volcanism/hydrothermalism) could be grossly underestimated.

Better understanding of the modern marine S cycle is also important for reconstructing past S cycle changes. An isotopic fractionation associated with microbial SO_4^{2-} re-

duction (MSR) typically depletes product aqueous sulfide in the rare heavy isotope ^{34}S (Kaplan & Rittenberg, 1964; Wing & Halevy, 2014). This ^{34}S-depletion is passed on to sulfide minerals that form an important marine output flux. The observed SO_4^{2-}-sulfide $\delta^{34}S$ offset has commonly been utilized create one-box steady-state model reconstructions of the relative amount of reduced S buried throughout Earth's history (Canfield, 2004; Kampschulte & Strauss, 2004; Canfield & Farquhar, 2009). Although recent work (Pasquier et al., 2017, 2021) has demonstrated local variability in this offset due to physical sedimentary parameters, few studies have interrogated the quantitative impacts of this variability on a global scale. Furthermore, studies of the offset across time (Leavitt et al., 2013; Wu et al., 2014) have relied almost exclusively on shelf sediments due to preservation biases in the geologic record and may underestimate the true magnitude of the offset if deep marine pyrite burial significantly affects isotope mass balance.

Here, we re-examine global SO_4^{2-} reduction and the diversity of sedimentary S cycling across deep ocean environments by applying cluster analysis to pore water [SO_4^{2-}] profiles from 700+ DSDP, ODP, and IODP sites. We subsequently construct a literature compilation of 300+ paired pyrite abundance + $\delta^{34}S$ measurements and 1200+ total sulfur abundance measurements from recent marine sediments to explore the coherence of sedimentary data with existing global nSRR estimates and the potential effects of depositional environment shifts on isotope mass balance in the marine S cycle.

2 Materials and Methods

2.1 Cluster analysis

To examine S cycling in deep ocean sediments across the globe, we downloaded data collected during previous DSDP, ODP, and IODP cruises from the JANUS (`http://iodp.tamu.edu/janusweb/links/links\_all.shtml`) and LIMS (`http://web.iodp.tamu.edu/LORE/`) databases. These data included all available geochemical data on interstitial waters, gases, and solid phases as well as physical properties data on sedimentary porosity. Once downloaded, data were imported into MATLAB® and saved into MATLAB® structures.

Applying *k*-means clustering to pore water profiles requires interpolation of all data to the same depth resolution over an identical depth interval. To enable cluster analysis, pore water [SO_4^{2-}] data were extracted from the structures and interpolated to an identical depth resolution of 1 m across all sites. Due to variation in the length of core over which pore water data were collected, we experimented with several bottom boundary depths to find an appropriate balance between the total number of profiles included in the analysis (which is reduced as the bottom boundary extends beyond the maximum depth of pore water data) and the length of the depth interval for clustering; our choice of a bottom boundary of 100 mbsf reduces the number of sites included in the analysis from 780 to 729, but makes the differences between the clusters more visually clear. Following interpolation, [SO_4^{2-}] data were inserted into a master array in which each row represented data from a different site and each column data from a specific depth (i.e., column 1 houses all [SO_4^{2-}] for 0 mbsf at different sites, column 2 houses 1 mbsf data, etc.). Sites with $<$ five pre-interpolation [SO_4^{2-}] data points or with no [SO_4^{2-}] data below the chosen bottom boundary were excluded from our analysis. Outlying [SO_4^{2-}] measurements differing more than 10 mM from measurements above and below the data point were also removed before clustering.

After creation of the master [SO_4^{2-}] array, we used MATLAB®'s evalclusters function to evaluate the optimal number of clusters based on the entries in the [SO_4^{2-}] array. We chose the optimal number of clusters by maximizing the Calinski-Harabasz Index (also known as the variance ratio index). This index ratios the overall variance (sum

of the squares) of observations between clusters to the variance within the clusters:

$$\text{Calinski-Harabasz Index} = \frac{SS_B}{SS_W} \text{ x } \frac{N-k}{k-1} \tag{3}$$

where SS_B is the variance between the clusters, SS_W is the variance within the clusters, N is the number of observations (sites in this case), and k is the number of clusters. Index values for totals of two to eight k-means clusters are depicted in Figure S1 and indicate an optimal number of four. Clustering was accomplished using MATLAB®'s kmeans function with a squared Euclidian distance metric and 1000 maximum iterations. Clusters were numbered such that the cluster with the most sites was designated as Cluster 1 and progressively less populated clusters were assigned chronologically increasing numbers. Use of other bottom boundary depths does not dramatically affect the results, as the clusters remain similar in terms of optimal number (3-6) and general character across the explored bottom boundary range (10 to 400 mbsf in 10 m increments).

Following clustering, water depth, porosity, total organic carbon (TOC) content, and calcium carbonate ($CaCO_3$) content data from the deep ocean drilling databases were extracted and examined to understand the controls on the [SO_4^{2-}] profiles across all sites. Sedimentation rates at each site were estimated based on water depth using an empirical relationship (Middelburg et al., 1997) as follows:

$$\omega = 10^{a+bZ} * CF \tag{4}$$

where ω is the sedimentation rate in cm/yr, a = -0.87478367, b = -0.00043512, Z is the water depth, and CF = 3.3. Mean aerial nSRRs at all sites were also estimated using the following equation (Canfield, 1991):

$$\text{Mean aerial nSRR} = \phi D_s \frac{dC}{dz} + \phi_o \omega C_o - \phi_b \omega C_b \tag{5}$$

Here, ϕ is the mean porosity within the zone of SO_4^{2-} reduction, D_s is the sedimentary diffusion coefficient for SO_4^{2-}, $\frac{dC}{dz}$ is the SO_4^{2-} concentration gradient with depth, ϕ_o is the initial phi at the sediment-water interface, ω is the sedimentation rate, C_o is the initial SO_4^{2-} concentration at the sediment-water interface, ϕ_b is the porosity at the base of the zone of SO_4^{2-} reduction, and C_b is the minimum SO_4^{2-} concentration (i.e., the SO_4^{2-} concentration at the base of the zone of SO_4^{2-} reduction). Porosities at various depths were calculated using a one- or two-term exponential fit to site porosity data with depth. SO_4^{2-} concentration gradients were estimated as follows:

$$\frac{dC}{dz} = \frac{\left([SO_4^{2-}]_o - [SO_4^{2-}]_b\right)}{z_b} \tag{6}$$

where $[SO_4^{2-}]_o$ is the SO_4^{2-} concentration at the sediment water interface, $[SO_4^{2-}]_b$ is the minimum SO_4^{2-} concentration, and z_b is the depth of the minimum SO_4^{2-} concentration. The SO_4^{2-} sedimentary diffusion coefficient was estimated assuming a constant molecular diffusion coefficient of 4.88 x 10^{-6} cm^2/s for SO_4^{2-} as follows:

$$D_s = \frac{D_o}{\phi^{1-n}} \tag{7}$$

where D_o is the molecular diffusion coefficient for SO_4^{2-} and n = 1.8 (Berner, 1980).

Absolute nSRRs in $mol/m^3/yr$ at different sediment depths were estimated using the following equation:

$$nSRR(z) = \frac{1}{\phi}\left[-D_s \frac{d(\phi \frac{dC}{dz})}{dz} + \frac{d(\phi \omega_c C_z)}{dz}\right] \tag{8}$$

Here, ω_c is the compaction-corrected solid phase burial rate at depth z and C_z is the corresponding SO_4^{2-} concentration. In this case, ϕ was estimated based on exponential fits

of shipboard measured porosity data with depth and $\frac{dC}{dz}$ was estimated by differentiating a spline fit to the shipboard $[SO_4^{2-}]$ data. ω_c was calculated as follows:

$$\omega_c = \omega \left(\frac{1 - \phi_f}{1 - \phi} \right) \tag{9}$$

where ϕ_f is the porosity value at the bottom depth in the exponential fit to the porosity data.

For estimating burial fluxes, initial porosity values for all DSDP, ODP, and IODP sites with data at depths < 5 mbsf were plotted and fitted with a linear regression against water depth after removing outliers. Initial porosities across the global ocean were then estimated by using this regression and the resulting values applied to ETOPO1 hypsometry grid points (Amante & Eakins, 2009) binned into 1 m depth bins. Sedimentation rates were similarly estimated by applying Equation 4 across the same depth increments. Surface areas represented by the ETOPO1 grid cells were calculated based on the latitude and longitude of grid cell boundaries (Kelly & Šavrič, 2021) and used to calculate average initial porosities and sedimentation rates within the shelf, slope, rise, and abyss depth classes; these averages were weighted by the estimated surface areas included within the associated 1 m depth bins.

2.2 Pyrite Compilation

To understand relationships among pyrite burial flux, pyrite $\delta^{34}S$, and water depth, we compiled literature measurements of pyrite abundance and $\delta^{34}S$ from marine sediments and imported the data into MATLAB®. Pyrite ages were estimated using published age models or by combining sediment depth information with sedimentation rates approximated from water depth (Middelburg et al., 1997). Abundance outliers and samples of > 40 Ma estimated age were removed from the compilation to reduce the influence of unrepresentative samples (e.g. pyrite nodules) and samples unlikely to have been deposited at water depths similar to modern. Pyrite S accumulation rates were estimated using pyrite abundance data, sedimentation rate estimates (Middelburg et al., 1997), and a linear fit of initial porosity data (from the JANUS and LIMS databases) with water depth. When unreported, water depths were in rare cases estimated based on published GPS coordinates or from locality maps within the corresponding studies.

3 Results

3.1 *k*-means clustering

Profiles for the optimal number of clusters (four) at a bottom boundary depth of 100 meters below seafloor (mbsf) are displayed in Figure 1 and are notably different. Profiles in the most populated cluster (Cluster 1; $n = 352$) show little decrease in $[SO_4^{2-}]$ with depth, consist with mostly oxic sedimentary conditions. In contrast, profiles in the second most populated cluster (Cluster 2; $n = 219$) feature relatively quick SO_4^{2-} depletion with depth, consistent with anaerobic oxidation of methane (AOM) in the upper part of the sediment. The centroid (i.e., within-cluster average) for this cluster shows that the average depth of complete SO_4^{2-} consumption is ~30 mbsf. Cluster 3 ($n = 153$) is intermediate in character between the two most populated clusters; profiles feature a slight $[SO_4^{2-}]$ decrease with depth and 100 mbsf $[SO_4^{2-}]$ typically well above zero, consistent with organoclastic MSR dominating the $[SO_4^{2-}]$ profiles. Profiles within the final cluster (Cluster 4; $n = 5$) are anomalous and show an increase in $[SO_4^{2-}]$ suggesting a source of SO_4^{2-} at depth within the sediments (Böttcher et al., 1998). As indicated by the slopes of the $[SO_4^{2-}]$ gradients, the mean nSRR within the clusters decreases such that Cluster 2 > Cluster 3 > Cluster 1.

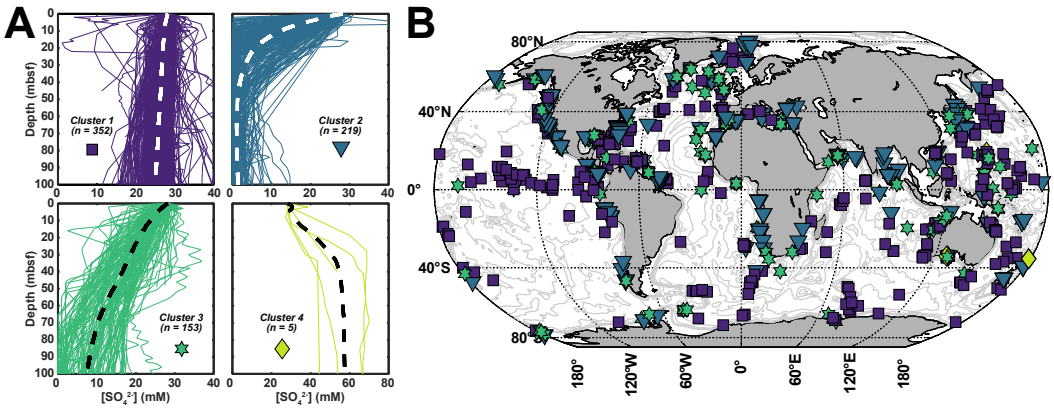

Figure 1. (A) $[SO_4^{2-}]$ depth profiles for 0 to 100 mbsf for sites within Clusters 1 to 4. Dashed lines denote the centroid for each cluster. (B) Global map of sites included within the cluster analysis. Symbol shape and color denote cluster assignment as indicated in (A). Map created using the M _Map mapping package (Pawlowicz, 2020).

Consideration of the geographic distribution of cluster sites (Figure 1B) yields further insight into cluster characteristics. While the relatively high nSRR sites of Clusters 2 and 3 are located predominantly in coastal regions, the low nSRR sites of Cluster 1 are more commonly found in the open ocean (Figure 1B). This preference is reflected in the median water depths for the sites within each cluster; while the median water depth for Cluster 1 sites is $\geq$~3000 meters below sea level (mbsl), the median depths for all other clusters are $\leq$~2500 mbsl. Cluster 4 sites are limited in their geographic distribution and are not depicted in this figure due to the low number of sites. The geographic disparity among the clusters is similarly mirrored by geochemical disparity, as demonstrated by differences in mean TOC and $CaCO_3$ contents among the sites (Figure S2).

3.2 Pyrite compilation

The relationship between pyrite S burial flux and pyrite $\delta^{34}S$ resulting from our literature compilation is shown in Figure 2. Pyrite $\delta^{34}S$ values vary by over 70‰ and estimated pyrite S accumulation rates range over six orders of magnitude across different marine environments. There is also some coherent structure to the variation; despite substantial scatter, the data show a trend toward lower $\delta^{34}S$ as accumulation rate decreases from the maximum plotted accumulation rate toward a rate of $\sim 10^{-3}$ mol/m^2/yr. While data at accumulation rates below 10^{-3} mol/m^2/yr are sparse, the apparent reversal of this trend at lower accumulation rates (Figure S3) could reflect rapid exhaustion of labile organic substrate and preservation of pyrite exclusively formed under more "closed-system" conditions (Sim et al., 2017).

Additional insight into the importance of different depositional environments can be gleaned from the relationship between water depth and $\Delta\delta^{34}S$, the difference between the $\delta^{34}S$ of seawater SO_4^{2-} and that of pyrite. Mean pyrite $\delta^{34}S$ weighted as a function of pyrite S accumulation rate increases with water depth, while simultaneously, mean sedimentary S concentrations for the same samples decrease with water depth (Figure 3). However, these data oversample productive coastal regions (Figure S3) with high S concentrations, as evidenced by an expansion of geographic coverage and reductions in mean S concentrations across nearly all water depth intervals when 1200+ additional measurements without isotopic data from PANGAEA are considered (Figure 3 & S4). Despite this bias, we suspect that the increase in $\Delta\delta^{34}S$ with water depth would remain in-

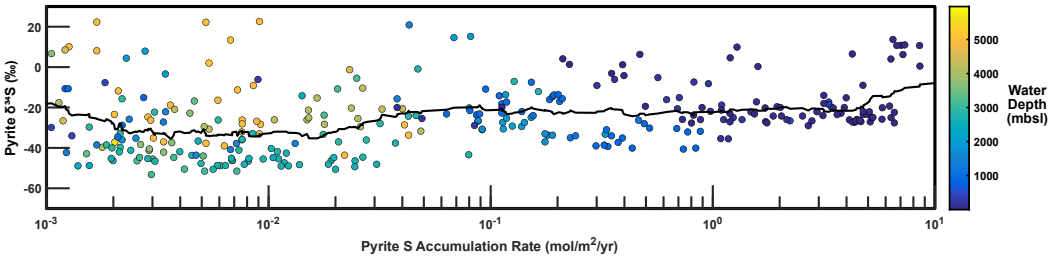

Figure 2. Literature compilation of 343 measurements (colored circles) of pyrite δ^{34}S plotted against estimated pyrite S accumulation rate. Color of symbols denotes modern water depth and solid black line denotes a 30-point moving average. Accumulation rates were estimated based on measured pyrite S content and sedimentation rate; rates ¡ 10^{-3} mol/m^2/yr (n = 32) and ¿ 10^{1} mol/m^2/yr (n = 1) are not shown due to low data density (¡ 20 per order of magnitude rate change). Sedimentation rates were taken from the literature or were estimated from water depth based on the relationship of (Middelburg et al., 1997). Data from (Alt & Burdett, 1992; Puchelt & Hubberten, 1980; Zak et al., 1980; Sweeney & Kaplan, 1980; Goldhaber & Kaplan, 1974; Scharff, 1980; Bonnell & Anderson, 1987; Böttcher et al., 2004; A. Migdisov et al., 1980; A. A. Migdisov et al., 1983; Lein et al., 1976; Krouse et al., 1977; Johnston et al., 2008; Vinogradov et al., 1962; Kaplan et al., 1963; Sweeney, 1972; Thode et al., 1960; Kaplan et al., 1960; Lein, 1983; Hartmann & Nielsen, 2012; A. A. Migdisov et al., 1974).

tact in a geographically unbiased data set given our weighting of the mean pyrite δ^{34}S by S accumulation rate (which accounts for the larger influence of sediments with high S concentrations on the δ^{34}S of the overall pyrite burial flux within each depth interval).

4 Discussion & Conclusions

k-means clustering identifies S cycle influences, but accurate prediction of nSRR at unsampled sites remains difficult

Our application of *k*-means clustering to deep sea drilling data has demonstrated its effectiveness at finding trends within large data sets in a less computationally complex manner than in previous work (Bowles et al., 2014). The geographic locations (Figure 1B) and geochemical statistics associated with the clusters (e.g. Figure S2) also underscore the strong influence of terrigenous input on MSR at a given site. Clusters with higher nSRRs are associated with higher TOC content, lower $CaCO_3$ content, and closer proximity to land than those with relatively low nSRRs. We note there is much less overlap among the clusters for TOC content than for $CaCO_3$ content and water depth, suggesting that TOC input is the primary control on the [SO_4^{2-}] profile at a given site.

The disparate mean TOC contents among the clusters (Figure S2) suggests some potential for the nSRR at a given site to be estimated from TOC data. However, plots of mean TOC content against water depth (Figure S5) and mean nSRR against mean TOC burial flux (Figure S6) show enough scatter to render such estimates highly imprecise; actual values routinely deviate by an order of magnitude or more from the best fit relationships to these data sets. Estimates could likely be improved through substitution of independently-measured sediment accumulation rates the addition of other reactive transport variables affecting sedimentary sulfur cycling (e.g. temperature, sedimentary iron content, and porosity) as independent variables.

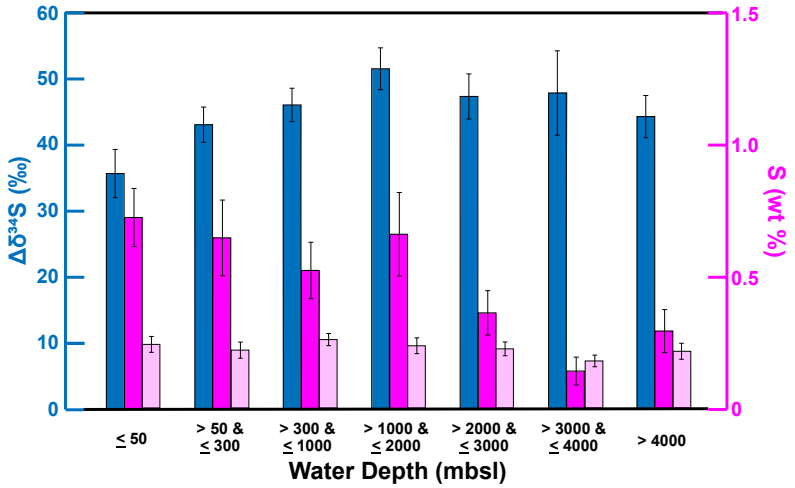

Figure 3. Average $\Delta\delta^{34}S$ between seawater SO_4^{2-} and pyrite (blue bars, left axis), average solid phase S concentration for samples with S isotopic measurements (magenta bars, right axis), and average solid phase S concentration for data including 1200+ samples without isotopic data (light pink bars, right axis) binned as a function of water depth. Error bars denote the 2σ standard error of the mean.

Mass balance calculations confirm a biased or incomplete assessment of the marine S cycle

Uncertainties in nSRR and other deep marine sedimentary parameters have important consequences for our understanding of isotope mass balance within the modern marine S cycle. To demonstrate this, we constructed a modified steady state isotope mass balance equation as follows:

$$\delta^{34}S_{in} = \delta^{34}S_{evap}(1 - f_{py,tot}) - (\Delta\delta^{34}S_{py,shelf} f_{py,shelf} + \Delta\delta^{34}S_{py,slope} f_{py,slope} + \Delta\delta^{34}S_{py,rise} f_{py,rise} + \Delta\delta^{34}S_{py,abyss} f_{py,abyss}) \quad (10)$$

where $\delta^{34}S_{in}$ is the $\delta^{34}S$ of the weathering input, $\delta^{34}S_{evap}$ is the $\delta^{34}S$ of buried sulfate evaporites (assumed to equal $\delta^{34}S_{sea}$, the $\delta^{34}S$ of seawater here), $f_{py,tot}$ is the total fraction of the input flux buried as pyrite, and the remaining terms are the $\Delta\delta^{34}S$ and pyrite burial fractions associated with shelf, slope, rise, and abyss sediments. We can also construct a simple sum of pyrite burial fluxes from individual depositional environment classes to obtain a total pyrite burial flux estimate:

$$F_{py,tot} = F_{py,shelf} + F_{py,slope} + F_{py,rise} + F_{py,abyss} \quad (11)$$

Using the averages from the S concentration compilation displayed in Figure 3, we assigned characteristic solid phase S concentrations (0.231±0.022, 0.250±0.018, 0.204±0.017, and 0.215±0.031 wt%; 2σ SE) and depth intervals (< 300, 300-2000, 2000-4000, and > 4000 mbsl) to shelf, slope, rise, and abyss depositional environments, respectively. We then used the ETOPO1 version of Earth's modern hyposometry (Amante & Eakins, 2009) to estimate the modern pyrite S burial flux out of Earth's oceans. After calculating initial porosities for each ETOPO1 depth bin based on water depth, assuming that

50±5% of shelf area constitutes permeable sands with no pyrite burial (Huettel et al., 2014), and incorporating the root mean squared errors of the regressions of sedimentation rate and initial porosity against water depth, we arrived at an estimated total pyrite S burial flux of 2.7 ± 1.3 (1σ) Tmol S/yr. The large uncertainty in this estimate originates almost exclusively from the sedimentation rate regression (Middelburg et al., 1997) and could be reduced through improved prediction of sedimentation rate from water depth. Irregardless, this estimate is within error of the riverine SO_4^{2-} input to seawater (2.8± 0.4 Tmol S/yr (Burke et al., 2018)) and is compatible with a marine S cycle in steady state. However, it is substantially higher than a prior estimate (1.2 Tmol S/yr; (Berner, 1982)). This disagreement and the implication that nearly all (∼96%) of the riverine input is being buried as reduced S suggests that biases remain. Comparison of the S burial fluxes with aerial nSRRs derived from the k-means clusters further supports remaining biases (Supporting Information).

One potential source of systematic bias in solid phase estimates of the reduced S burial flux is sediment porosity. Although sediment porosity data are commonly collected in deep sea drilling efforts, disturbance during the coring process can easily lead to loss or compaction of core material (Morton & White, 1997). Such processes would cause the in-situ porosity of recovered samples to be underestimated by post-coring measurements and the corresponding solid phase-based burial estimates to be overestimated. Applying a linear regression between initial porosity and water depth that instead considers the maximum initial porosity in a 50-point moving window with water depth (Figure S7) lowers the pyrite burial flux estimate to 0.87±0.41 Tmol S/yr. This burial flux is now within error of the prior estimate of 1.2 Tmol S/yr (Berner, 1982). While an inaccurate estimate of the hydrothermal flux remains possible, this finding and preliminary comparison of deep sea drilling porosity data with similar multi-core data (Figure S7) strongly suggests biased porosity measurements contribute to the high burial flux estimate. An increase in dissolved-phase output flux estimates due to such a porosity bias suggests sampling and analytical biases better explain the high global nSRR estimate of (Bowles et al., 2014) (Supporting Information).

Assignment of characteristic $\Delta\delta^{34}S$ values to the aforementioned depth intervals allows for further assessment of fluxes and isotope mass balance in the marine S cycle. Assuming characteristic pyrite $\delta^{34}S$ values of −15.2‰, −25.3‰, −26.1‰, and −23.1‰ and $f_{py,i}$ values of 0.46, 0.35, 0.155, and 0.035 for the shelf, slope, rise, and abyss (respectively), equation 10 yields a steady state seawater SO_4^{2-} $\delta^{34}S$ value of +17.3‰ assuming a pyrite burial flux of 0.87 Tmol S/yr ($f_{py,tot} = 0.31$) and +28.7‰ if a pyrite burial flux of 1.3 Tmol S/yr ($f_{py,tot} \sim 0.45$, the maximum value considered likely in a prior study (Tostevin et al., 2014)) is imposed; the sulfate evaporite burial flux is assumed equal to the pre-anthropogenic riverine input (2.8 Tmol S/yr, $\delta^{34}S_{in} = +4.6$‰ (Burke et al., 2018)) minus the pyrite burial flux in each case. The bracketing of the measured modern seawater $\delta^{34}S$ of +21.24‰ (Tostevin et al., 2014) by these values is encouraging and suggests general accuracy in both the pyrite burial flux magnitudes in each depositional environment and their isotopic composition. If $\delta^{34}S_{in}$ remains unchanged, equation 10 can yield a seawater $\delta^{34}S$ value in agreement with the observed value if (1) $f_{py,tot} \sim 0.37$ (pyrite burial flux = 1.03 Tmol S/yr) and the pyrite $\delta^{34}S$ values are kept the same; (2) one or more of the $\Delta\delta^{34}S$ values is increased while keeping $f_{py,tot} \sim 0.31$ (pyrite burial flux = 0.87 Tmol S/yr); (3) one or more of the $\Delta\delta^{34}S$ values is decreased while keeping $f_{py,tot} \sim$ 0.45 (pyrite burial flux = 1.3 Tmol S/yr); or some intermediate combination of 1-3. We favor scenario (3) given the absence of deltaic sediments with closed-system S diagenesis and high pyrite $\delta^{34}S$ in our $\delta^{34}S$ compilation and the relatively close match between the corresponding pyrite burial flux and Berner's (1982) independently-derived value (1.2 Tmol S/yr). Increasing the shelf pyrite $\delta^{34}S$ by about 17‰ to +2.0‰ (i.e., lowering the total $\Delta\delta^{34}S$ to +34.0‰) is sufficient to match the observed seawater $\delta^{34}S$ in this case.

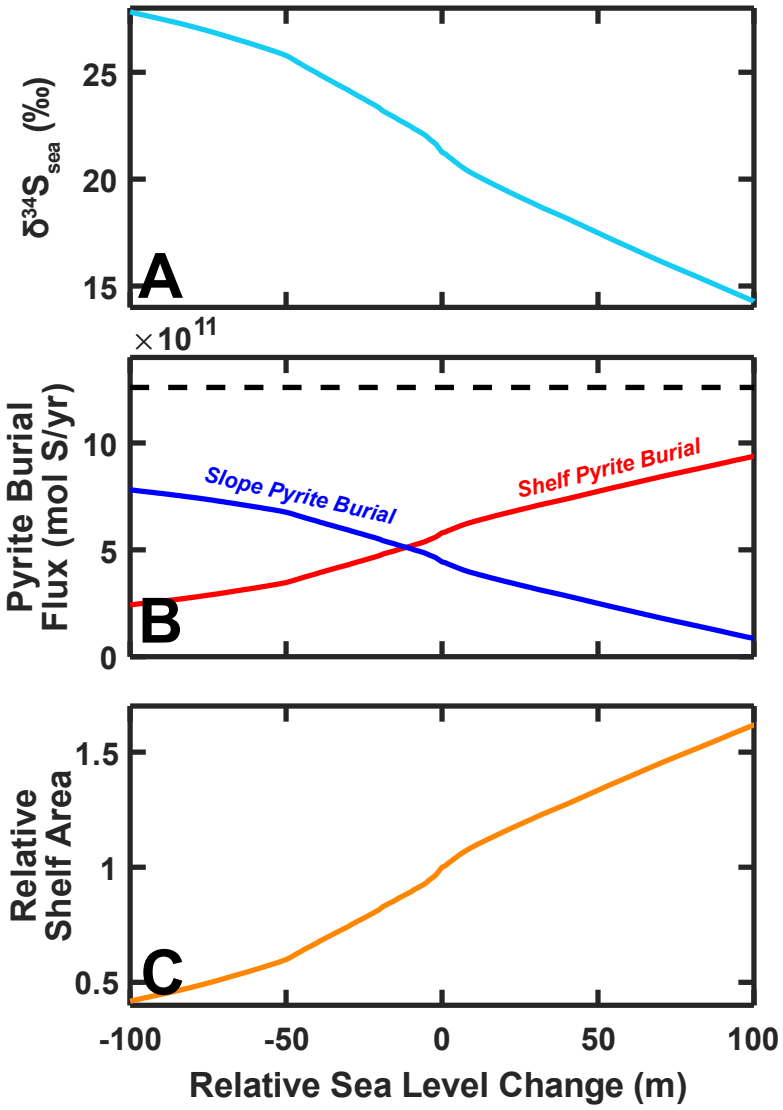

Figure 4. (A) Calculated steady-state seawater $\delta^{34}S$ for shelf $\Delta\delta^{34}S$ = 19.2 and slope $\Delta\delta^{34}S$ = 46.5‰. (B) Continental shelf (red), continental slope (blue), and total (black dashed) pyrite burial fluxes. (C) Calculated change in the amount of submerged shelf area (0-300 mbsl) relative to modern for a given change in sea level.

Seawater $\delta^{34}S$ is sensitive to pyrite burial locii changes

In the mass balance scenarios considered here, nearly half of pyrite burial in the modern ocean occurs in shelf sediments. However, prior work (Berner, 1982) has discussed a possible transfer of some shelf sedimentation to the deep ocean in conjunction with lower sea levels during the last glacial period. Burial of pyrite in proportion to sedimentation would concomitantly shift some shelf pyrite burial to deeper environments in this scenario. How would such a transfer affect S isotope mass balance?

To estimate the sensitivity of seawater $\delta^{34}S$ to sedimentation shifts, we used the ETOPO1 arc-minute global relief model (Amante & Eakins, 2009) to determine the approximate change in shelf area for changes in sea level (SL) ranging from -100 m to +100

m (Figure 4) and transferred sedimentation between the shelf and slope in proportion to the relative shelf area change. An $f_{\mathrm{py,tot}}$ of 0.45 was imposed to meet the constraints of a previous estimate of $f_{\mathrm{py,tot}}$ (Tostevin et al., 2014) and modify the characteristic shelf pyrite δ^{34}S to +2.0‰. We also assume that the characteristic $\Delta\delta^{34}$S values remain constant as sea level changes and plot the results in Figure 4. Note that modern global hypsometry is dominated by topography near sea level: a sea level decrease of just 50 m halves the shelf area, while an increase of 50 m augments shelf area by ∼50% (Figure 4C). Shifting pyrite burial without changing shelf or slope $\Delta\delta^{34}$S causes the steady-state seawater δ^{34}S to change by over 6‰ for a 100 m rise or fall in sea level (Figure 4A). Augmenting the modern $f_{\mathrm{py,shelf}}$ or the difference between shelf and slope pyrite δ^{34}S increases the sensitivity to sea level, while lowering this difference or decreasing the overall $f_{\mathrm{py,tot}}$ dampens the sensitivity. Changes in $\Delta\delta^{34}$S within environments could also partially offset such shelf-area related effects in real-world scenarios. Although Pleistocene sea level changes are too frequent for this mechanism to force substantial seawater δ^{34}S changes given the 10+ Myr modern seawater SO_4^{2-} residence time (Walker, 1986), the mechanism could plausibly alter seawater δ^{34}S on longer (1 Myr+) timescales (Leavitt et al., 2013; Rennie et al., 2018; Johnson et al., 2020) or at times with much lower seawater $[SO_4^{2-}]$ (Lowenstein et al., 2003).

5 Open Research

All data and associated MATLAB files used to conduct this study have been archived within the Zenodo repository (`doi:10.5281/zenodo.6415289`; this DOI has been reserved and the files will be uploaded here upon acceptance, but are included here as supplementary material here for review. The "Description.txt" file includes the description that will be used for the Zenodo item.). The SO_4^{2-} concentration and porosity data used for cluster analysis in this study are freely available from the International Ocean Discovery Program's JANUS (`http://iodp.tamu.edu/janusweb/links/links\_all.shtml`) and LIMS (`http://web.iodp.tamu.edu/LORE/`) databases and were organized into structures in the MATLAB workspace file "DeepSeaSO4_ClusterAnalysisData.mat" included in the repository. Paired pyrite sulfur abundance and isotopic composition data for this paper are compiled in Dataset S1 ("DatasetS1.xlsx") from many corresponding references (Alt & Burdett, 1992; Puchelt & Hubberten, 1980; Zak et al., 1980; Sweeney & Kaplan, 1980; Goldhaber & Kaplan, 1974; Scharff, 1980; Bonnell & Anderson, 1987; Böttcher et al., 2004; A. Migdisov et al., 1980; A. A. Migdisov et al., 1983; Lein et al., 1976; Krouse et al., 1977; Johnston et al., 2008; Vinogradov et al., 1962; Kaplan et al., 1963; Sweeney, 1972; Thode et al., 1960; Kaplan et al., 1960; Lein, 1983; Hartmann & Nielsen, 2012; A. A. Migdisov et al., 1974). Additional total sulfur abundance and porosity data are freely available from the PANGAEA database (`https://www.pangaea.de/`) under Creative Commons 3.0 Unported (CC-BY-3.0) licenses (`https://creativecommons.org/licenses/by/3.0/`); the data and corresponding DOI links are included in the "POROSITY.mat" MATLAB workspace file. Full text citations to both the pyrite S abundance and porosity compilation data sources are listed in PDF files included at the DOI link. Additional information about the files may be found in the description at the associated DOI.

References

Alt, J. C., & Burdett, J. W. (1992). Sulfur in Pacific deep-sea sediments (Leg 129) and implications for cycling of sediment in subduction zones. In *Proc. ODP, Sci. Results* (Vol. 129, pp. 283–294). College Station, TX (Ocean Drilling Program).

Amante, C., & Eakins, B. W. (2009). ETOPO1 arc-minute global relief model: procedures, data sources and analysis.

Berner, R. A. (1980). *Early Diagenesis: A Theoretical Approach.* Princeton Uni-

versity Press. Retrieved 2017-12-03, from https://press.princeton.edu/titles/121.html

Berner, R. A. (1982). Burial of organic carbon and pyrite sulfur in the modern ocean: its geochemical and environmental significance. *Am. J. Sci*, *282*(4), 451–473.

Berner, R. A. (2005, July). The carbon and sulfur cycles and atmospheric oxygen from middle Permian to middle Triassic. *Geochimica et Cosmochimica Acta*, *69*(13), 3211–3217. Retrieved 2018-10-01, from http://www.sciencedirect.com/science/article/pii/S0016703705002553 doi: 10.1016/j.gca.2005.03.021

Bonnell, L. M., & Anderson, T. F. (1987). SULFUR ISOTOPIC VARIATIONS IN NODULAR AND DISSEMINATED PYRITE-HOLE-603B. *Initial Reports of the Deep Sea Drilling Project*, *93*, 1257–1262.

Bowles, M. W., Mogollón, J. M., Kasten, S., Zabel, M., & Hinrichs, K.-U. (2014, May). Global rates of marine sulfate reduction and implications for sub–sea-floor metabolic activities. *Science*, *344*(6186), 889–891. Retrieved from http://www.sciencemag.org/content/344/6186/889.abstracthttp://www.sciencemag.org/content/344/6186/889.full.pdf doi: 10.1126/science.1249213

Burke, A., Present, T. M., Paris, G., Rae, E. C. M., Sandilands, B. H., Gaillardet, J., ... Adkins, J. F. (2018, August). Sulfur isotopes in rivers: Insights into global weathering budgets, pyrite oxidation, and the modern sulfur cycle. *Earth and Planetary Science Letters*, *496*, 168–177. Retrieved 2020-07-18, from http://www.sciencedirect.com/science/article/pii/S0012821X18302991 doi: 10.1016/j.epsl.2018.05.022

Böttcher, M. E., Brumsack, H. J., & de Lange, G. J. (1998). Sulfate reduction and relation stable isotope (34S, 18O) variations in interstitial waters from the Eastern Mediterranean. *Proceedings of the Ocean Drilling Program, Scientific Results*, *160*, 365–373.

Böttcher, M. E., Khim, B.-K., Suzuki, A., Gehre, M., Wortmann, U. G., & Brumsack, H.-J. (2004, April). Microbial sulfate reduction in deep sediments of the Southwest Pacific (ODP Leg 181, Sites 1119–1125): evidence from stable sulfur isotope fractionation and pore water modeling. *Marine Geology*, *205*(1), 249–260. Retrieved from http://www.sciencedirect.com/science/article/pii/S002532270400026X doi: 10.1016/S0025-3227(04)00026-X

Canfield, D. E. (1991, February). Sulfate reduction in deep-sea sediments. *American journal of science*, *291*(2), 177–188. Retrieved from http://europepmc.org/abstract/MED/11538491http://www.ajsonline.org/cgi/content/abstract/291/2/177http://dx.doi.org/10.2475/ajs.291.2.177http://www.ajsonline.org/cgi/reprint/291/2/177.pdfhttp://www.ajsonline.org/content/291/2/177.full.pdf doi: 10.2475/ajs.291.2.177

Canfield, D. E. (2004, December). The evolution of the Earth surface sulfur reservoir. *American Journal of Science*, *304*(10), 839–861. Retrieved from http://www.ajsonline.org/content/304/10/839.abstracthttp://www.ajsonline.org/content/304/10/839.full.pdf doi: 10.2475/ajs.304.10.839

Canfield, D. E., & Farquhar, J. (2009, May). Animal evolution, bioturbation, and the sulfate concentration of the oceans. *Proceedings of the National Academy of Sciences*, *106*(20), 8123–8127. Retrieved from http://www.pnas.org/content/106/20/8123.abstracthttp://www.pnas.org/content/106/20/8123.full.pdf doi: 10.1073/pnas.0902037106

Goldhaber, M. B., & Kaplan, I. R. (1974). The Sulfur Cycle. In E. D. Goldberg (Ed.), *The Sea* (Vol. 5, pp. 569–655). New York, NY: Wiley.

Hartmann, M., & Nielsen, H. (2012, March). 34S values in recent sea sediments and their significance using several sediment profiles from the western Baltic Sea. *Isotopes in Environmental and Health Studies*, *48*(1), 7–32. Retrieved

2018-08-15, from https://doi.org/10.1080/10256016.2012.660528 doi: 10.1080/10256016.2012.660528

Huettel, M., Berg, P., & Kostka, J. E. (2014). Benthic Exchange and Biogeochemical Cycling in Permeable Sediments. *Annual Review of Marine Science*, *6*(1), 23–51. Retrieved 2021-12-02, from https://doi.org/10.1146/annurev-marine-051413-012706 (_eprint: https://doi.org/10.1146/annurev-marine-051413-012706) doi: 10.1146/annurev-marine-051413-012706

Johnson, D. L., Grossman, E. L., Webb, S. M., & Adkins, J. F. (2020, September). Brachiopod 34SCAS microanalyses indicate a dynamic, climate-influenced Permo-Carboniferous sulfur cycle. *Earth and Planetary Science Letters*, *546*, 116428. Retrieved 2020-07-07, from http://www.sciencedirect.com/science/article/pii/S0012821X20303721 doi: 10.1016/j.epsl.2020.116428

Johnston, D. T., Farquhar, J., Habicht, K. S., & Canfield, D. E. (2008). Sulphur isotopes and the search for life: strategies for identifying sulphur metabolisms in the rock record and beyond. *Geobiology*, *6*(5), 425–435. Retrieved 2018-07-09, from https://onlinelibrary.wiley.com/doi/abs/10.1111/j.1472-4669.2008.00171.x doi: 10.1111/j.1472-4669.2008.00171.x

Kampschulte, A., & Strauss, H. (2004). The sulfur isotopic evolution of Phanerozoic seawater based on the analysis of structurally substituted sulfate in carbonates. *Chemical Geology*, *204*(3–4), 255–286. Retrieved from http://www.sciencedirect.com/science/article/pii/S0009254103003747http://ac.els-cdn.com/S0009254103003747/1-s2.0-S0009254103003747-main.pdf?_tid=4c8c7d50-3e8f-11e4-99f8-00000aab0f01&acdnat=1410974771_d9c820b720005816b666f68d8d9245f7http://ac.els-cdn.com/S0009254103003747/1-s2.0-S0009254103003747-main.pdf?_tid=d58ccd76-eee3-11e4-b8e7-00000aab0f27&acdnat=1430362483_2890e4c59cfbdee9094655020ac04f2d doi: 10.1016/j.chemgeo.2003.11.013

Kaplan, I. R., Emery, K. O., & Rittenbebg, S. C. (1963, April). The distribution and isotopic abundance of sulphur in recent marine sediments off southern California. *Geochimica et Cosmochimica Acta*, *27*(4), 297–331. Retrieved from http://www.sciencedirect.com/science/article/pii/0016703763900747 doi: 10.1016/0016-7037(63)90074-7

Kaplan, I. R., Rafter, T. A., & Hulston, J. R. (1960). SULPHUR ISOTOPIC VARIATIONS IN NATURE. PART 8. APPLICATION TO SOME BIOGEOCHEMICAL PROBLEMS. *New Zealand J. Sci.*, *3*.

Kaplan, I. R., & Rittenberg, S. C. (1964, February). Microbiological Fractionation of Sulphur Isotopes. *Journal of General Microbiology*, *34*(2), 195–212. Retrieved from http://mic.sgmjournals.org/content/34/2/195.abstracthttp://mic.sgmjournals.org/content/34/2/195.full.pdf doi: 10.1099/00221287-34-2-195

Kelly, K., & Šavrič, B. (2021). Area and volume computation of longitude–latitude grids and three-dimensional meshes. *Transactions in GIS*, *25*(1), 6–24. Retrieved 2022-03-02, from https://onlinelibrary.wiley.com/doi/abs/10.1111/tgis.12636 (_eprint: https://onlinelibrary.wiley.com/doi/pdf/10.1111/tgis.12636) doi: 10.1111/tgis.12636

Krouse, H. R., Brown, H. M., & Farquharson, R. B. (1977, April). Sulphur isotope compositions of sulphides and sulphates, DSDP Leg37. *Canadian Journal of Earth Sciences*, *14*(4), 787–793. Retrieved 2018-06-27, from http://www.nrcresearchpress.com/doi/abs/10.1139/e77-078 doi: 10.1139/e77-078

Leavitt, W., Halevy, I., Bradley, A., & Johnston, D. (2013). Influence of sulfate reduction rates on the Phanerozoic sulfur isotope record. *Proceedings of the National Academy of Sciences of the United States of America*, *110*(28), 11244–9. Retrieved from http://sfx.caltech.edu:8088/caltech?sid=google&auinit=WD&aulast=Leavitt&atitle=Influence%20of%

20sulfate%20reduction%20rates%20on%20the%20Phanerozoic%20sulfur%20isotope%20record&id=pmid%3A23733944http://www.ncbi.nlm.nih.gov/pmc/articles/PMC3710818/pdf/pnas.201218874.pdf

Lein, A. Y. (1983). Biogeochemistry of the Anaerobic Diagenesis of Recent Baltic Sea Sediments. *Ecological Bulletins*(35), 441–461. Retrieved 2019-09-23, from https://www.jstor.org/stable/20112879

Lein, A. Y., Kudryavtseva, A., Matrosov, A. G., & Zyakun, A. M. (1976). Isotopic composition of sulfur compounds in sediments of the Pacific. *Biochemistry of Diagenesis of Ocean Sediments, Nauka, Moscow*, 179–185.

Lowenstein, T. K., Hardie, L. A., Timofeeff, M. N., & Demicco, R. V. (2003, October). Secular variation in seawater chemistry and the origin of calcium chloride basinal brines. *Geology*, *31*(10), 857–860. Retrieved from http://geology.gsapubs.org/content/31/10/857.abstract doi: 10.1130/g19728r.1

Middelburg, J. J., Soetaert, K., & Herman, P. M. J. (1997, February). Empirical relationships for use in global diagenetic models. *Deep Sea Research Part I: Oceanographic Research Papers*, *44*(2), 327–344. Retrieved 2019-10-15, from http://www.sciencedirect.com/science/article/pii/S096706379600101X doi: 10.1016/S0967-0637(96)00101-X

Migdisov, A., Galimov, E., Grinenko, V., Barskaya, N., & Krivitsky, V. (1980, June). 32. MAJOR AND MINOR ELEMENTS AND SULFUR ISOTOPES OF THE MESOZOIC AND CENOZOIC SEDIMENTS AT SITES 415 AND 416, LEG 50, DEEP SEA DRILLING PROJECT. doi: 10.2973/dsdp.proc.50.132.1980

Migdisov, A. A., Belyi, V. M., Barskaja, N. V., & Grinenko, V. A. (1983). 18. The Concentration and Isotope Composition of Sulfur from the Galapagos Mounds Area Sediments, Leg 70, Deep Sea Drilling Project.

Migdisov, A. A., Cherkovskiy, S. L., & Grinenko, V. A. (1974). The effects of formation conditions on the sulfur isotopes of aquatic sediments. *Geochemistry International*, *11*, 1028–1047.

Morton, R. A., & White, W. A. (1997). Characteristics of and Corrections for Core Shortening in Unconsolidated Sediments. *Journal of Coastal Research*, *13*(3), 761–769. Retrieved 2021-12-08, from https://www.jstor.org/stable/4298671 (Publisher: Coastal Education & Research Foundation, Inc.)

Pasquier, V., Bryant, R. N., Fike, D. A., & Halevy, I. (2021, February). Strong local, not global, controls on marine pyrite sulfur isotopes. *Science Advances*, *7*(9), eabb7403. Retrieved 2021-03-08, from https://advances.sciencemag.org/content/7/9/eabb7403 (Publisher: American Association for the Advancement of Science Section: Research Article) doi: 10.1126/sciadv.abb7403

Pasquier, V., Sansjofre, P., Rabineau, M., Revillon, S., Houghton, J., & Fike, D. A. (2017, June). Pyrite sulfur isotopes reveal glacialinterglacial environmental changes. *Proceedings of the National Academy of Sciences*, *114*(23), 5941–5945. Retrieved from http://www.pnas.org/content/114/23/5941.abstract doi: 10.1073/pnas.1618245114

Pawlowicz, R. (2020). *M_map: A mapping package for MATLAB.* Retrieved from https://www.eoas.ubc.ca/~rich/map.html

Puchelt, H., & Hubberten, H.-w. (1980). 39. Preliminary Results of Sulfur Isotope Investigations on Deep Sea Drilling Project Cores From Legs 53 and 53. In *Initial Reports on the Deep Sea Drilling Project* (Vol. 51-53, pp. 1145–1148).

Rennie, V. C. F., Paris, G., Sessions, A. L., Abramovich, S., Turchyn, A. V., & Adkins, J. F. (2018, October). Cenozoic record of 34 S in foraminiferal calcite implies an early Eocene shift to deep-ocean sulfide burial. *Nature Geoscience*, *11*(10), 761–765. Retrieved 2018-10-01, from https://www.nature.com/articles/s41561-018-0200-y doi: 10.1038/s41561-018-0200-y

Scharff, M. L. (1980). *Die Verteilung von Stickstoff, Schwefel, Schwefel-Isotopen sowie Mn, Zn, Fe und Cu in Sedimenten des Atlantischen Ozeans (DSDP-*

Bohrkerne) (Unpublished doctoral dissertation). Uitgever niet vastgesteld.

Sim, M. S., Paris, G., Adkins, J. F., Orphan, V. J., & Sessions, A. L. (2017, June). Quantification and isotopic analysis of intracellular sulfur metabolites in the dissimilatory sulfate reduction pathway. *Geochimica et Cosmochimica Acta*, *206*, 57–72. Retrieved 2020-05-25, from http://www.sciencedirect.com/science/article/pii/S0016703717301187 doi: 10.1016/j.gca.2017.02.024

Sweeney, R. E. (1972). *Pyritization during Diagenesis of Marine Sediments* (Unpublished doctoral dissertation). University of California Los Angeles, Los Angeles.

Sweeney, R. E., & Kaplan, I. R. (1980, June). Diagenetic sulfate reduction in marine sediments. *Marine Chemistry*, *9*(3), 165–174. Retrieved from http://www.sciencedirect.com/science/article/pii/0304420380900353 doi: 10.1016/0304-4203(80)90035-3

Thode, H. G., Harrison, A. G., & Monster, J. (1960). Sulphur Isotope Fractionation in Early Diagenesis of Recent Sediments of Northeast Venezuela. *AAPG Bulletin*, *44*(11), 1809–1817. Retrieved 2018-06-27, from http://archives.datapages.com/data/bulletns/1957-60/data/pg/0044/0011/1800/1809.htm

Torres, M. A., West, A. J., & Li, G. (2014). Sulphide oxidation and carbonate dissolution as a source of CO2 over geological timescales. *Nature*, *507*(7492), 346–349. Retrieved from http://dx.doi.org/10.1038/nature13030http://www.nature.com/nature/journal/v507/n7492/pdf/nature13030.pdf doi: 10.1038/nature13030

Tostevin, R., Turchyn, A. V., Farquhar, J., Johnston, D. T., Eldridge, D. L., Bishop, J. K. B., & McIlvin, M. (2014). Multiple sulfur isotope constraints on the modern sulfur cycle. *Earth and Planetary Science Letters*, *396*(0), 14–21. Retrieved from http://www.sciencedirect.com/science/article/pii/S0012821X1400209Xhttp://ac.els-cdn.com/S0012821X1400209X/1-s2.0-S0012821X1400209X-main.pdf?_tid=df7a2150-8ae6-11e4-bbf0-00000aab0f01&acdnat=1419368672_7edf368fd7843474b99fb40219b21b71 doi: 10.1016/j.epsl.2014.03.057

Vinogradov, A. P., Grinenko, V. A., & Ustinov, V. I. (1962). Isotopic composition of sulfur compounds in the Black Sea. *Geochemistry*, *10*, 973–997.

Walker, J. C. G. (1986, February). Global geochemical cycles of carbon, sulfur and oxygen. *Marine Geology*, *70*(1), 159–174. Retrieved from http://www.sciencedirect.com/science/article/pii/0025322786900939 doi: 10.1016/0025-3227(86)90093-9

Wing, B. A., & Halevy, I. (2014, October). Intracellular metabolite levels shape sulfur isotope fractionation during microbial sulfate respiration. *Proceedings of the National Academy of Sciences*. Retrieved from http://www.pnas.org/content/early/2014/10/30/1407502111.abstracthttp://www.pnas.org/content/early/2014/10/30/1407502111http://www.pnas.org/content/111/51/18116.full.pdf doi: 10.1073/pnas.1407502111

Wu, N., Farquhar, J., & Strauss, H. (2014). 34S and 33S records of Paleozoic seawater sulfate based on the analysis of carbonate associated sulfate. *Earth and Planetary Science Letters*, *399*(0), 44–51. Retrieved from http://www.sciencedirect.com/science/article/pii/S0012821X14002982http://ac.els-cdn.com/S0012821X14002982/1-s2.0-S0012821X14002982-main.pdf?_tid=6d478bf2-4862-11e4-93e0-00000aab0f02&acdnat=1412055010_09a8c5edee21707f00ec160e8807a516 doi: 10.1016/j.epsl.2014.05.004

Zak, I., Sakai, H., & Kaplan, I. R. (1980). Factors controlling the 18O/16O and 34S/32S isotope ratios of ocean sulfates, evaporites and interstitial sulfates from modern deep sea sediments. *Isotope marine chemistry*, 339–373.